Identification of Stop Criteria for Large-Scale Laboratory Slab Tests Using Digital Image Correlation and Acoustic Emission

Christensen, Christian Overgaard; Zhang, Fengqiao; Garnica, Gabriela Zarate; Lantsoght, Eva Olivia Leontien; Goltermann, Per; Schmidt, Jacob Wittrup

Article

Identification of Stop Criteria for Large-Scale Laboratory Slab Tests Using Digital Image Correlation and Acoustic Emission

Christian Overgaard Christensen [1,*], Fengqiao Zhang [2], Gabriela Zarate Garnica [2], Eva Olivia Leontien Lantsoght [2,3], Per Goltermann [1] and Jacob Wittrup Schmidt [4]

[1] Department of Civil Engineering, Technical University of Denmark, 2800 Kongens Lyngby, Denmark; pg@byg.dtu.dk
[2] Concrete Structures, Delft University of Technology, 2628 CD Delft, The Netherlands; F.Zhang-5@tudelft.nl (F.Z.); G.I.ZarateGarnica@tudelft.nl (G.Z.G.); E.O.L.Lantsoght@tudelft.nl (E.O.L.L.)
[3] Colegio de Ciencias e Ingenierías, Universidad San Francisco de Quito, Quito 170901, Ecuador
[4] Department of Built Environment, University of Aalborg, 9220 Aalborg, Denmark; jws@build.aau.dk
[*] Correspondence: coch@byg.dtu.dk; Tel.: +45-27-103333

Abstract: Advanced monitoring methods are required to identify stop criteria in proof-load tests. In this study, the combined methodology of two-dimensional digital image correlation and acoustic emission is investigated for its applicability for future implementation in field tests. The two monitoring systems are deemed to provide valuable insight with external measurements from digital image correlation and internal measurements from acoustic emission. Two overturned T-section reinforced concrete slabs ($0.37 \times 1.7 \times 8.4$ m) tested under laboratory conditions are used for the assessment. The first slab test served as a preliminary test to enable sensor placement and creation of a relevant loading protocol. The main scientific results lead to a proposal for a test procedure using the combined methodology based on results, observations, and experiences from an individual stop criteria assessment for the two methods. The results include full-field plots, an investigation of the time of crack detection and monitoring of crack widths with digital image correlation, and a qualitative assessment of activity vs. load followed by a quantitative evaluation of calm ratios using acoustic emission. The individual results show that both digital image correlation and acoustic emission can identify damage occurrence earlier than other secondary methods. At crack detection (415 kN), crack widths were measured at widths between 0.078 mm to 0.125 mm and can be monitored until reaching the stop criterion at 463 kN (Eurocode SLS threshold of $w_{max} = 0.2$ mm). The acoustic emission results were limited by the pre-defined loading protocol and thus, only indicated that damage occurred sometime between 300 kN and 500 kN (pre-defined load levels). Therefore, the proposal for test procedure involves a methodology, where the loading protocol may be updated during testing based on monitoring results and thus provide even more valuable data.

Keywords: crack evaluation; digital image correlation; proof-loading; concrete slab bridges; stop criteria; acoustic emission; repeated loading; load cycles; load history

1. Introduction

Load-carrying capacity assessment of existing concrete slab bridges through load testing is a topic of growing interest among bridge owners. Many existing concrete slab bridges were built in the 1960s and 1970s, and these are not designed for the actual traffic loads of today. Several studies involving capacity evaluations have been conducted during the last decades to evaluate the actual in-situ capacity compared to theoretical predictions [1–4]. Many of these studies have shown that a capacity reserve may be present for a high number of bridge structures [5–9]. Based on the gained insight, it seems that load testing may be a good option for more accurate evaluations [10]. Three types of in-situ bridge load testing are typically used to evaluate the structural response; (1) Diagnostic load testing, (2) Proof-load testing, and (3) Failure load testing [11], see [12] for flowcharts

specifically associated with the methods of diagnostic load testing and proof-load testing. Proof-loading methods are of particular interest when assessing the ability of existing bridges to carry the code-prescribed live loads. However, a demand is that load testing methods must include full control of the test procedure and the bridge response during testing to high load levels, safeguarding that no irreversible structural damage may occur. To achieve this, a proof-loading is governed by certain monitoring-based thresholds, also called stop criteria.

An extensive review of existing monitoring methods was performed by [13]. The study presented in the current paper has a particular focus dedicated to the combination of digital image correlation (DIC) and acoustic emission (AE) for identification of stop criteria. In [13], DIC is highlighted for its advantages of non-contact, full-field measurements and having no fixed reference. AE is highlighted for real-time measurements of fracture processes and its high sensitivity. In practical application, DIC offers external measurements, while AE provides internal measurements. Both methods provide global measurements and are thus not limited to point measurements like many conventional methods. The authors deem the combination an excellent stop criteria assessment tool with significant potential for application in proof-load testing. The methods have, therefore, been chosen for this study [14,15].

Hypothesis and Research Questions

It is hypothesized that the combined methodology of DIC and AE can provide robust stop criteria identification, and thus may be used as a solid monitoring package when performing proof-load testing. AE is, in this regard, deemed to support DIC by adding internal structural information on crack identification and damage assessment through load and calm ratios to DIC results on crack detection, development, and crack widths. To the authors' knowledge, no previous research studies have, in this way, applied the combined methodology on concrete slabs of comparable size. The study may thus illuminate the scientific potential of the method and provide an increased solid basis for further research. The following research questions are relevant to consider for the study:

- Can DIC and AE be used to identify relevant stop criteria effectively?
- May the combined methodology be used to improve the obtained results of the individual methods?
- Is it possible to implement qualitative and quantitative observations and measurements to obtain more robust results?
- Can existing test methods be optimized towards the combined methodology and its implementation in field testing?

2. Literature Review

A proof-load test of a bridge is considered successful if the bridge can withstand the target proof-load without signs of distress. The target proof-load is defined as representative of the factored live load and is applied in the desired critical positions. If the target proof-load is reached without exceeding the stop criteria, the test is successful. If stop criteria are reached before reaching the target proof-load, the bridge capacity and class must be adjusted accordingly.

In recent studies in Denmark [16], the target load has been defined based on the Danish classification system used for the administration and control of heavy vehicles [17,18]. Axle load configuration, position, and load magnitude are described for every bridge class. These can thus be applied according to the guideline in combination with given safety factors. A Danish guideline on bridge proof-load testing is currently under development based on this classification system.

A proof-load test also has to involve monitoring-based stop criteria to identify signs of distress in the structure. Such criteria may consist of crack detection, crack width monitoring, crack distribution, strain distributions, changes in stiffness, or other unique sets of parameters. However, the guidelines on this topic are limited. Several national guidelines

exist for diagnostic, and proof-loading of structures, e.g., [19,20], but knowledge related to bridge testing stop criteria needs to be implemented. The existing guidelines either use general terms without specifying values for stop criteria or are limited in application and are, therefore, insufficient.

Recent work has combined ideas from existing guidelines in a proposal for flexural stop criteria for concrete bridges [21]. This proposal involves methods for calculating stop criteria using structural information, while earlier stop criteria thresholds were set to fixed values, such as the German guideline [19] and the Eurocode demands for SLS [22]. At this point, the method does not involve pre-stressed concrete structures and is thus limited to non-prestressed steel reinforced concrete. Similarly, stop criteria related to brittle failures such as shear failure mechanisms are still under further development [23–29].

Even though research provides a sound basis for future stop criteria, providing a sufficient safety level during and after proof-loading through identification of robust stop criteria is an open research topic [30]. A challenge often encountered when dealing with existing bridges is that a low documentation level may result in insufficient theory-based calculations. More qualitative approaches may, in this case, be needed to identify stop a criteria [31]. An example of such a qualitative stop criterion is the identification of surface cracks or early crack activity. Recent studies have shown how DIC can be an effective tool for full-field monitoring [16,31–34], and thus be a beneficial method for both crack detection and crack width monitoring. Although not applied in this study, fiber optic sensing is another promising tool which can involve strain and crack monitoring [35–38].

As a support to DIC results, stiffness change may also be monitored through load/deflection data using the proposal by [21]; this can be done independently from other measured parameters. It is an important assessment parameter since stiffness change may be a precursor to irreversible damage following a transfer from the linear elastic stage to the plastic stage.

AE monitors unique parameters different from typical stop criteria. Most monitoring systems offer external measurements, whereas AE monitors acoustic activity internally in the tested structure. Experiments have shown that AE may detect cracking earlier than typical methods, including DIC [39]. However, AE has the drawbacks of lower accuracy in estimating crack locations and difficulties in quantifying crack openings. Therefore, combining AE with displacement measurements is deemed to provide more accurate results, which can be used efficiently in a package of multiple independent monitoring sources [30]. Multiple monitoring sources are essential in the safety assessment of proof-load testing, especially when applying a qualitative approach to stop criteria [30,31]. If two monitoring systems show indications of the same phenomenon, the reliability of the results increases dramatically. However, the applicability and relevance of any monitoring system must be considered for application in proof-load testing where amplified monitoring does not necessarily provide better data.

2.1. Digital Image Correlation

The use of digital image correlation is not new, and numerous studies have been performed on its precision and experimental applications [40,41]. However, most studies consider small-scale laboratory applications, where environmental conditions and other factors are more easily managed. For an in-situ application, the conditions are more challenging, and the precision may not be as expected; it may even vary from case to case. Recent studies have shown how two-dimensional DIC may be highly relevant in large-scale in-situ tests even though noise and other errors are present [16,31,33,34,42]. In [31], it is shown how cracks can be detected early in the load/deflection curve, after which crack widths can be monitored towards quantitative stop criteria. The results seem to present a solid basis for application in proof-load tests; however, the quantitative aspects of the study, including the definition of the threshold values, require further verification through the use of additional monitoring and tests on different concrete slab structures.

2.2. Acoustic Emission

The general term of acoustic emission involves phenomena where transient elastic waves are generated by the release of energy from a localized source [43]. This method thus differs from typical stop criteria identification, but shows promising results for damage assessment. The method has been applied in laboratory conditions for several years [44,45]; however, implementation for in-situ load tests is rarely seen [43,46]. It is possible to estimate the source location of AE hits, classify crack type, and identify damage levels. Typical AE analysis tools [47,48] may provide:

- Identification of the presence of the Kaiser or Felicity effect;
- Assessment of damage states using the Load and Calm ratios;
- Estimation of crack location, including zonal localization and source localization;
- Classification of the damage modes using AE signal features.

The Kaiser and Felicity effects are well-known concepts in AE evaluation. The Kaiser effect represents the absence of significant AE activity, and the Felicity effect, the presence of significant AE activity until the previously applied load level is exceeded. The load ratio is related to concepts from the Kaiser effect and can be used to assess the damage state along with the calm ratio, and these were suggested by [44]. The load ratio is given by the load of AE activity onset divided by the previous maximum load (see Equation (1)). If the Kaiser effect is present, AE activity onset is identical to the previous maximum load, and the structure may be considered sound; otherwise, some degree of damage may be present.

$$Load\ ratio = \frac{AE\ onset\ load}{Maximum\ load} \begin{cases} = 1,\ Sound \\ < 1,\ Damaged \end{cases} \tag{1}$$

The calm ratio is defined by the cumulative number of hits during unloading divided by the total number of hits during the whole cycle (see Equation (2)). Ohtsu et al. found that AE activity during unloading was limited for a stable structure, resulting in a calm ratio around zero [44]. This phenomenon and the associated damage identification can be described by the calm ratio.

$$Calm\ ratio = \frac{Hits(unload)}{Hits(load + unload)} \begin{cases} \to 0,\ Sound \\ > 0,\ Damaged \end{cases} \tag{2}$$

The load and calm ratios do not describe the actual damage state, only whether damage is present. Damage characterization can be obtained by combining the two ratios as proposed by Ohtsu et al., where the damage state can be quantified as minor, intermediate, and heavy using two threshold values (see Figure 1).
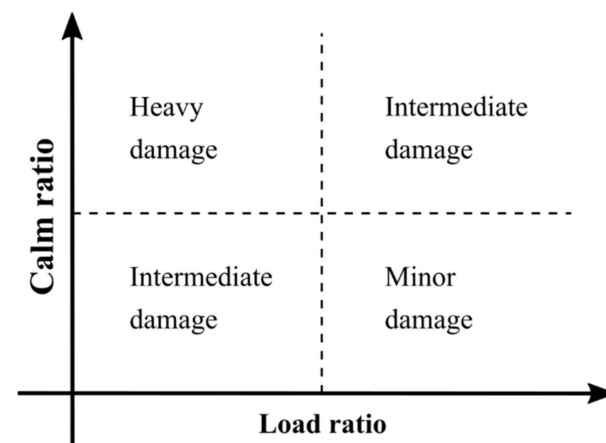

Figure 1. Damage classification by load and calm ratio [44].

The damage level is severe for a low load ratio and high calm ratio. The threshold values vary in the literature; load ratio 0.9 and calm ratio 0.05 are used in [44], 0.85 and 0.2 are used in [47], based on the Rilem TC-212-ACD recommendation [45], and the method has been further expanded to involve more groups and multiple ratios for the Ruytenschild Bridge in [46].

In order to enable the described AE analysis, a load test must involve repetition of load cycles and studies of load history. In many cases, the cyclic loading protocol described in the ACI 437.2M-13 [20] is ideal for AE measurements [43].

Preparation and installation are required before use in a proof-load test. In addition, due to limited range of the sensors (typically maximum 1 m, depending on signal attenuation), it may be challenging to monitor an entire slab surface, such as a concrete slab bridge. Therefore, it may be beneficial to have prior structural knowledge, such as capacity evaluations and structural response results from preliminary or diagnostic tests. With such information, sensors can be placed strategically and thus increase the amount of gained information. In addition, the analysis can be performed on a global level using all AE sensors or on individual sensors to obtain local information on regions of interest. Most AE systems facilitate real-time monitoring, where more advanced analysis typically is limited to post-analysis, including more accurate source localization and classification [39].

2.3. Combined Use of Digital Image Correlation and Acoustic Emission

Combined use of DIC and AE is hypothesized to provide a robust monitoring basis for stop criteria evaluations. Measurements performed with AE may provide an earlier warning in terms of microcracking, as well as crack and damage characterization and localization. DIC response evaluations and crack patterns provide thus an excellent basis for AE sensor placing. In previous studies, the combined use of DIC and AE have been shown to be an effective tool [14,15,39,49–52], but only few studies consider larger test specimens. Omondi et al. [14] tested on pre-stressed railway sleepers (2500 mm), but again with a local monitoring zone. Similar for all mentioned studies is that the crack propagation is studied far into the damaged states. In a proof-loading, however, a particular interest is on early crack identification and activation of stop criteria, which is not considered. In addition, none of the studies with combined DIC and AE consider the use of the load and calm ratio to characterize damage.

A rare example of the application of the combined methodology on large-scale specimens is presented by Zhang et al. (2020) [39], where parts of a bridge girder were tested (length between 10 and 12 m). DIC was used for full-field as well as local monitoring, and a large grid of AE sensors was applied. It is shown how microcracking may reveal crack formation prior to definite DIC detection, but also that the two independent systems were able to detect cracking at an early stage of the loading. In addition, the analysis involved AE source localization and crack classification as well as DIC analyses of crack kinematics and aggregate interlocking.

3. Large-Scale Laboratory Tests of OT-Slabs

The test specimens used for the experiments were constructed with down-scaled versions of Overturned T-section (OT) beams from an OT-slab bridge, tested in situ in 2017 [16,31]. The beams were down-scaled to 2/3 of the cross-sectional dimensions of the in-situ bridge, thus resulting in a width of 246 mm, a height of 300 mm, while a length of 8400 mm was chosen. The reinforcement ratio was kept the same. Seven beams were used for the OT-slabs, resulting in a total dimension of $8400 \times 1722 \times 370$ mm, including additional top concrete. The cross-section of a specimen is depicted in Figure 2, along with the reinforcement and concrete specifications.
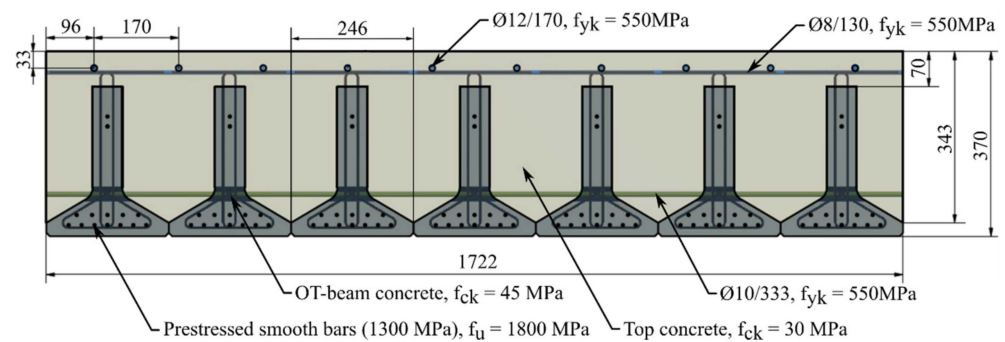
Figure 2. OT test specimen cross-section, all units in mm.

3.1. Test Setup and Monitoring

The test setup is depicted in Figure 3. The slabs were tested upside-down to better facilitate the tests and monitoring setup. The load-carrying support system consisted of 14 load-carrying columns with three stiffeners and three supporting I-profiles mounted on the columns with friction clamps. The supporting conditions (supported along three edges and one free edge) were set up as pinned supports (cradle bearings) and ensured a high shear transfer between the beam elements.
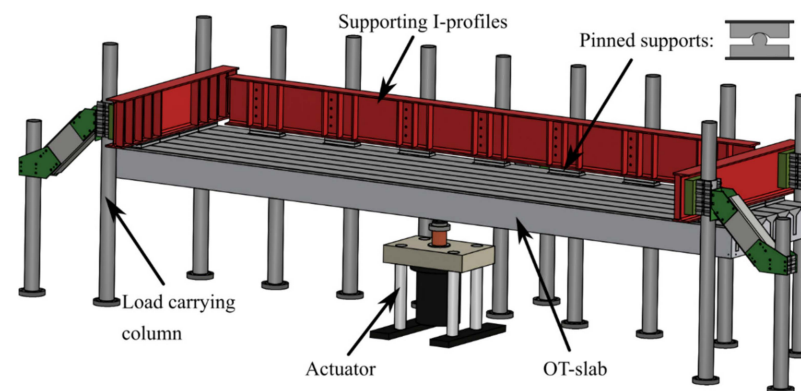
Figure 3. Large-scale OT-slab experimental setup.

The loading was applied as a point load at mid-span between beam number two and three (from the bottom) by a deformation-controlled hydraulic actuator with a capacity of 2 MN. The load was distributed to approximately 350×450 mm using a load distribution plate (see Figure 4). The described test setup gives a transverse span of 1599 mm and a longitudinal span of 7569 mm, also depicted in the figure.

Figure 4. DIC coverage and loading point. All units in mm.

A monitoring rig was constructed around the test setup to ensure that the sensors were not affected by test setup deformations (see Figure 5). LVDTs, distance lasers, and wire potentiometers were used to measure deflection, whereas strain gauges were used to measure strain in the transverse reinforcement. Full-field surface evaluation of deformations and cracks was achieved through the use of 2D DIC. The coverage of the primary DIC camera, a Canon 6D with 20 Mpx resolution camera, and 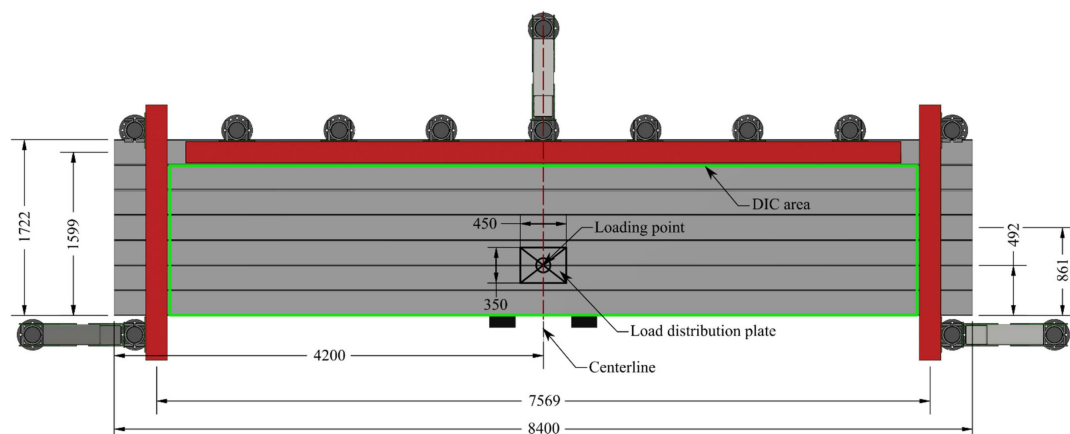a wide-angle lens (Canon EF 16–35 mm f/2.8L II USM) is seen in Figure 4. The camera distance was 3.8 m for both cameras, which correlates with earlier in-situ bridge tests [16,31], and images were captured every 10 s. The surface was covered in a contrast pattern, and apart from overhead laboratory lighting, no additional lighting was applied.
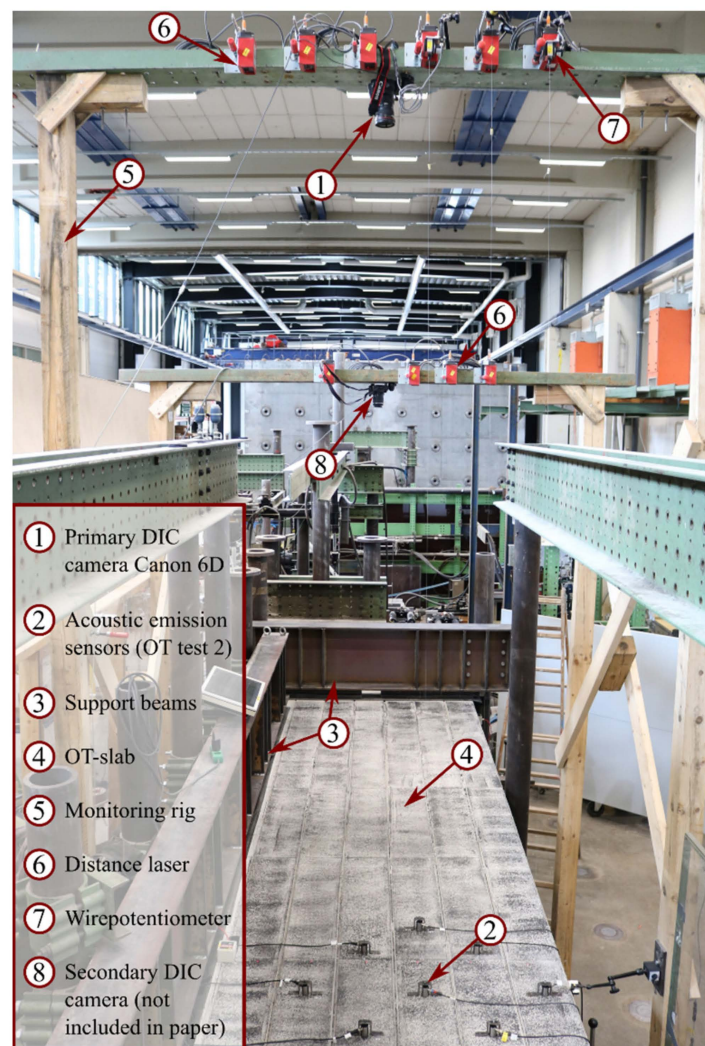
Figure 5. Test setup and monitoring sensors.

The current study involves post-processing results from a commercial software (GOM) [53]. However, during testing, an open-source software (Ncorr) [54] was applied for real-time updating of the DIC results. The software has been set up for such application by use of a loop for continuous updating.

In OT test 2, AE sensors were mounted on both the slab's top and bottom surfaces (see Figure 6). The sensors were of the type R6I with a central frequency of 60 kHz [55], and MISTRAS software AEwin [56] was used for analysis during the test. Steel holders were used to fix the sensors (see Figure 6), and an electrical compound was used as couplant between the sensors and concrete surface.

Figure 6. AE sensors mounted on top and bottom surfaces and LVDTs on the bottom surface.

The sensors were arranged according to the crack pattern from OT test 1, with sensor spacing determined based on a preliminary measurement of wave propagation. The sensor layout is depicted in Figure 7, where the sensor spacing is shown by the illustration of a sensor grid with a spacing of 250 mm and 246 mm. The distance between top and bottom sensors corresponds to the slab thickness of 370 mm.

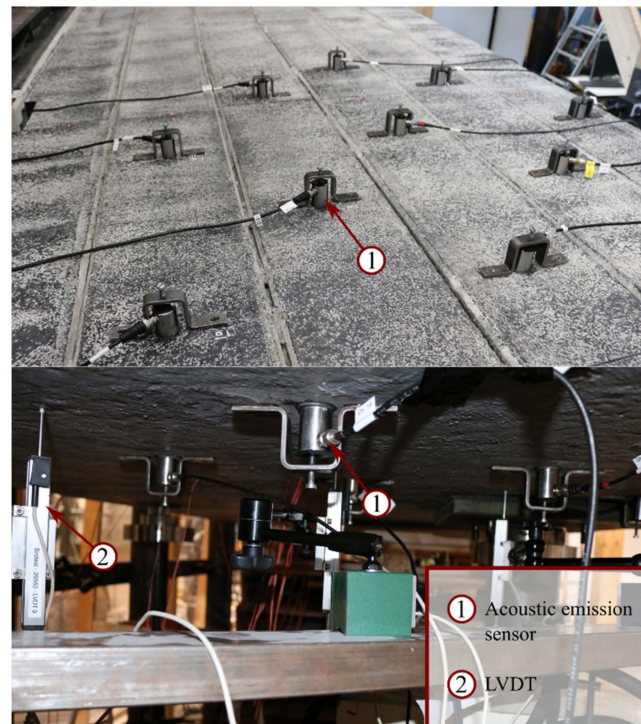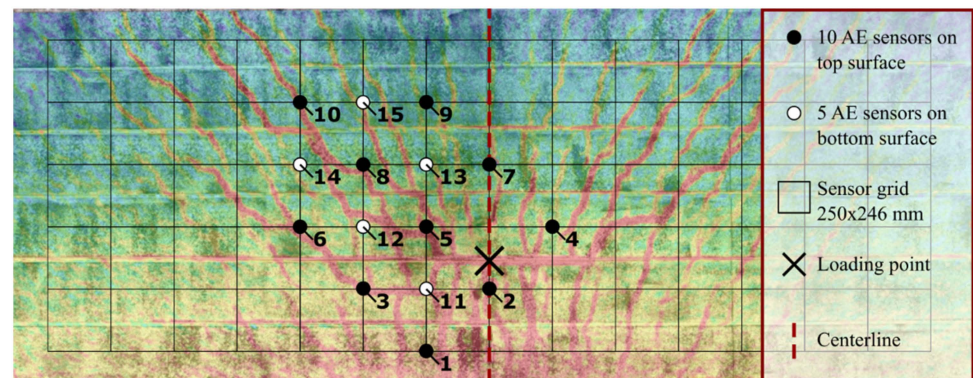**Figure 7.** AE sensor plan based on the crack pattern of OT test 1.

Before load testing, a preliminary measurement on wave propagation properties was performed. Fourteen sensors were installed in two lines, with one line of seven sensors on the top surface and the other of seven sensors on the bottom surface (Figure 8a). The first AE transducer emitted a pulse, which the other sensors received. The arrival time and peak amplitude of the received signals can then be derived. Based on the arrival times at different sensors, the wave speed was estimated to be 4400 m/s (Figure 8b). Figure 8c shows the drop of peak amplitude in dB. The measured peak amplitude here was mainly from surface waves. According to formulae on wave attenuation [57], the attenuation of surface waves and P-waves are estimated as the black and red dashed lines, respectively. P-waves would attenuate around 45 dB after 1 m. Supposing a source amplitude of 100 dB and a noise level of 55 dB, the signal could not be received after 1 m. With this information,

the maximum sensor spacing should be within 1 m to ensure that a sufficient number of sensors can receive the signals. The sensor spacing in the OT test (maximum 370 mm) is then within the requirements.

Figure 8. Preliminary test on wave propagation: (**a**) the fourteen sensors on top and bottom surfaces, (**b**) estimation of wave speed from arrival times, and (**c**) estimation of wave attenuation from amplitude drop.

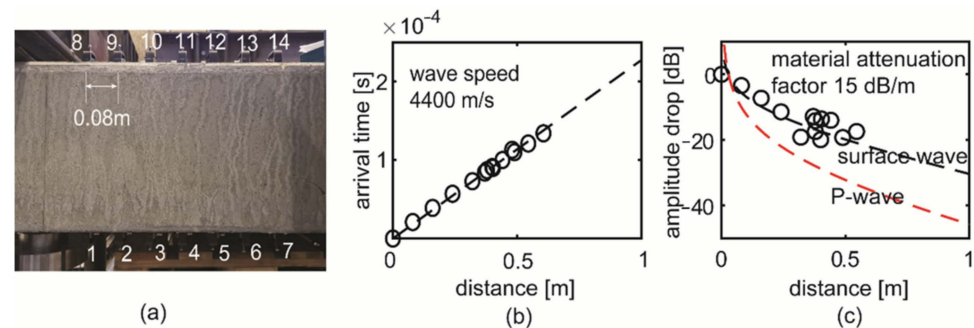### 3.2. Loading Protocol for OT Test 2

OT test 1 was a static failure load test performed with a load rate of 1 mm/min. In this test, crack detection was achieved at 413 kN, and yield lines developed between 620 kN and 750 kN, and the peak load was 819 kN [31]. Based on the experienced response curve and DIC crack observations, a loading protocol is designed for OT test 2. The aim of the loading protocol is to have three repeated loadings to three different stages of crack development. These are followed by one loading segment to the second load level and loading to failure, see Figure 9.
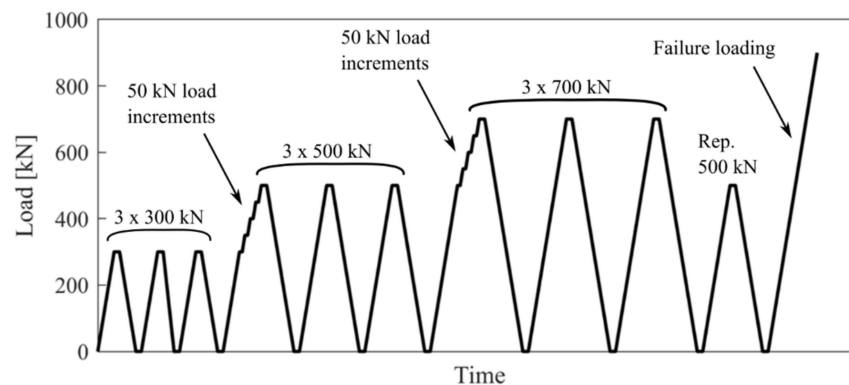
Figure 9. Loading scheme. Three load segments to 300 kN (before detectable cracking), three load segments to 500 kN (after crack detection), three load segments to 700 kN (developed cracks and plastic deformation), one load segment to 500 kN before loading to failure.

The three load levels used for the loading protocol are; (1) before detectable cracking (300 kN), (2) after crack detection (500 kN), and (3) developed cracking and plastic deformation (700 kN). The load is applied with the deformation-controlled load rate of 1 mm/min. When loading for the first time from 300 kN to 500 kN and 500 kN to 700 kN, load increments of 50 kN are applied, and a short hold of the load of 1 min is performed on each load peak to allow the cracking activity to stabilize. The load levels can not directly be associated with the Danish classification system, but for reference, the highest axle load in the system, corresponding to a class 500 t vehicle, is 23.7 t (236 kN) split into two wheel loads of 11.85 t (118 kN).

4. Test Results

Following OT test 1 as a preliminary test, OT test 2 was performed according to the designed loading protocol for evaluation of the combined use of DIC and AE. The achieved loading for OT test 2 is shown Figure 10. Comparing this with the desired loading protocol Figure 9, it is seen that the loading was successful. The achieved loading deviates slightly at higher load levels, which is expected due to stiffness change, plastic deformation, and long-term effects.
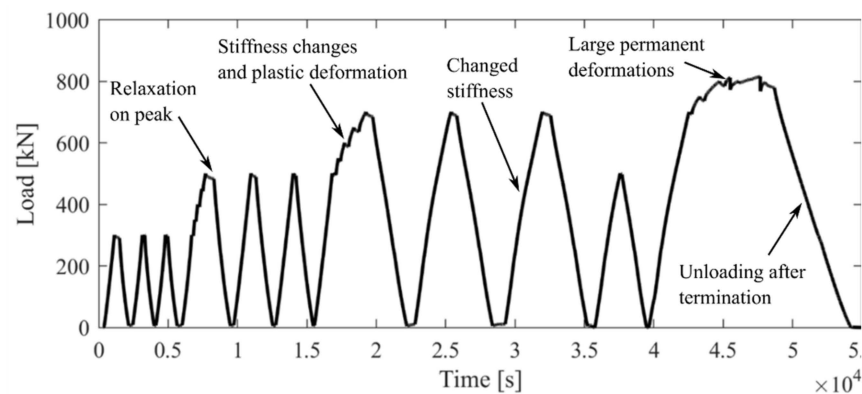
Figure 10. The achieved loading scheme.

4.1. Response Curve and Loading Segments

The response curves of OT test 1 and 2 are compared in Figure 11. It is seen how the overall response of OT test 2 follows the response of OT test 1, even though a more advanced loading protocol with repeated loading was applied.
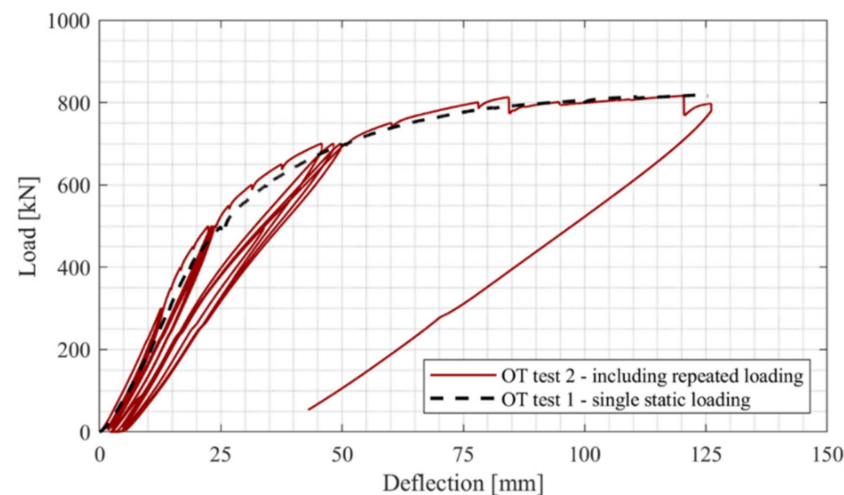
Figure 11. Test response curves.

At the peak load of 819 kN, there was a corresponding deflection of 125 mm for OT test 1. For OT test 2, these values were 816 kN and 126 mm, respectively. Similar crack formation and crack patterns were observed to evolve and grow, especially between 500 kN and 700 kN, after which the plastic regime continued until termination of the tests. Through a comparison to standard vehicles in the Danish classification system [18], it is seen that there is a significant capacity reserve in the OT-slabs [31].

4.1.1. Evaluation of Loading Segments

The results from Figure 11 show a reasonable linearity for both the 300 kN and 500 kN load levels. The maximum deflection on each load peak is seen in Table 1. Some non-linearity is quite common for large-scale tests with advanced structural compositions

and exposure to long-term effects and high magnitude loading [16]. The increase in deflection for the 500 kN load level is thus not necessarily a sign of non-linearity, and in a traditional proof-loading situation, this may not be cause for termination of the test.

Table 1. Maximum deflection development at the loading point for all load cycles.

Load Level		Maximum Deflection [mm]
300 kN	Cycle 1	12.7
	Cycle 2	13.0
	Cycle 3	13.1
500 kN	Cycle 1	22.4
	Cycle 2	23.2
	Cycle 3	23.6
700 kN	Cycle 1	45.8
	Cycle 2	48.2
	Cycle 3	49.7
500 kN		33.9
Failure (816 kN)		126.0

At the 700 kN load level, significant additional permanent deflection is generated with each loading cycle, and this is an indicator of a damaged state of the structure. The maximum deflection increases by 3.9 mm between load cycles one and three, and additionally, the maximum deflection at the following 500 kN load cycle is 10.3 mm larger than in cycle three of the 500 kN load segments. At this point, the structure is irreversibly damaged.

4.1.2. Stiffness Change

The theoretical method suggested by [21] has been used to evaluate the stiffness change. The method consists on evaluating the reduction of stiffness in the loading and unloading branches. The criterion limits the reduction of stiffness to 25% less than the original stiffness. Figure 12 shows the results from the reduction of stiffness. In the figure, the dashed line indicates the 25% reduction limit. It can be observed that the limit was reached in between load steps 6 and 7 for both branches. This means that during a proof load test, the load would have been stopped at load step 7, which corresponds to 700 kN (see Table 1).
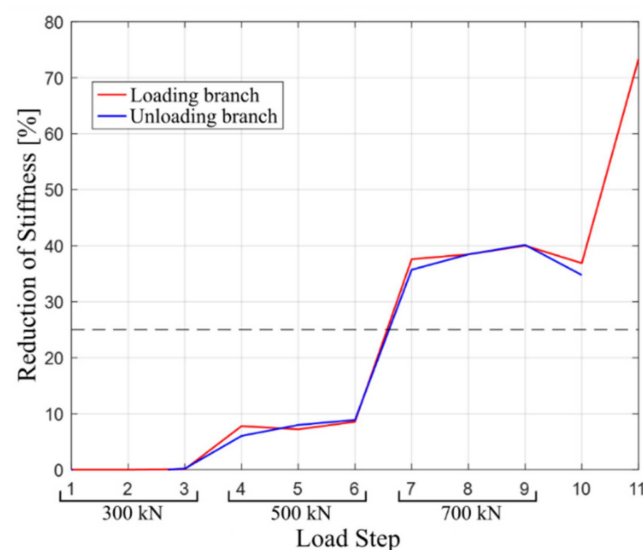

Figure 12. Reduction of stiffness loading and unloading branches per load step.

4.2. Digital Image Correlation

4.2.1. Crack Detection

Crack identification is performed using the methodology in [31]. With the applied image rate (1/10 s), the deformation controlled load rate of 2 mm/min, and with the stiffness level observed near crack detection, there is approximately 4 kN between the captured images. In OT test 1, the first crack was detected through DIC by visual identification in the processed DIC-image at 413 kN, see Table 2. Indications of cracking activity were present at 395 kN, but not enough for absolute identification. In OT test 2, the repeated loading enables assessment and evaluation of load history and its effect on crack detection. The results from OT test 2 shows that the crack detection load level is comparable to the results from OT test 1 on the first load cycle to 500 kN. Once the cracks have formed and some permanent deformation has manifested, the cracks can be detected at a significantly earlier stage for the following load cycles.

Table 2. Crack detection load levels.

Test	First Loading (500 kN)		Second Load Cycle (500 kN)	Third Load Cycle (500 kN)
	Crack Indications	Crack Detection		
OT test 1	395 kN	413 kN	-	-
OT test 2	399 kN	415 kN	325 kN	316 kN

4.2.2. Crack Pattern Development

The crack patterns for the third cycle of the three load levels and the repeated loading to 500 kN are shown in Figure 13. The plots provide qualitative information on the damage state of OT-slab 2 at each load level. It is seen how no cracking is visible for 300 kN and how early bending and separation cracks are visible for 500 kN. At 700 kN, yield lines form, and horizontal cracking occurs in the middle of individual beam elements. With the repetition of 500 kN, it is seen that the crack pattern differs significantly from the earlier 500 kN loading and is more similar to the 700 kN crack pattern. This indicates that the loading to 700 kN has significantly damaged the structure. A loading protocol with additional load levels and repetition of load levels could have provided additional information, e.g., between the 500 kN and 700 kN load levels.
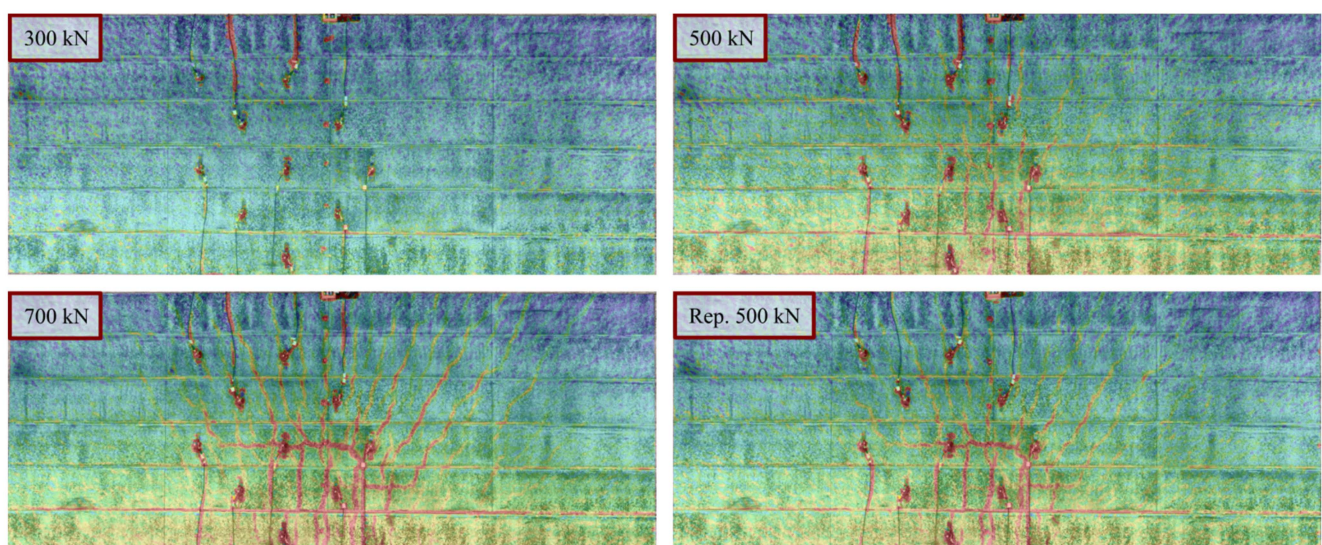

Figure 13. Crack patterns for the third load cycle of the three primary load levels and repetition of the second load level to 500 kN.

4.2.3. Crack Width for Each Unique Loading Segment

To further assess the damage state through DIC, crack widths have been evaluated. As significant damage seems to occur between the 500 kN and 700 kN load levels, focus is directed towards the three load peaks of the 500 kN load levels and to the time of the first crack detection (415 kN). The repeated loading to 500 kN is included for comparison and damage assessment. These are hypothesized to have a higher relevance for the further proof-loading and stop criteria assessment. The crack widths of six chosen cracks are listed in Table 3, both with and without correction for out-of-plane movement according to [31,33,34,42]. The validity of the crack width corrections was verified through control measurements in areas without any cracks, where any corrected crack width should be approximately equal to zero. The six chosen cracks and measured crack widths are also shown in Figure 14 for the first crack formation at 415 kN and at the third peak of the 500 kN load cycle. It is seen how noise may affect the distinguishing of individual cracks at the early crack detection, whereas the cracks are clearly defined at the third peak at 500 kN.

Table 3. Measured and corrected crack widths for three primary cracks on crack detection and all three load peaks of the 500 kN load cycles.

Crack No.	First Crack (415 kN)		Peak 1 (500 kN)		Peak 2 (500 kN)		Peak 3 (500 kN)		Repeated (500 kN)	
	$w_{measured}$ [mm]	$w_{corrected}$ [mm]	$w_{measured}$ [mm]	$w_{corrected}$ [mm]	$w_{measured}$ [mm]	$w_{corrected}$ [mm]	$w_{measured}$ [mm]	$w_{corrected}$ [mm]	$w_{measured}$ [mm]	$w_{corrected}$ [mm]
1	0.196	0.079	0.296	0.134	0.302	0.131	0.356	0.181	0.524	0.282
2	0.182	0.086	0.288	0.152	0.300	0.159	0.312	0.167	0.583	0.376
3	0.213	0.109	0.418	0.271	0.417	0.264	0.426	0.269	1.045	0.821
4	0.260	0.125	0.375	0.184	0.383	0.184	0.487	0.283	0.749	0.458
5	0.186	0.115	0.262	0.161	0.251	0.143	0.305	0.195	0.503	0.335
6	0.150	0.078	0.184	0.081	0.248	0.138	0.235	0.122	0.421	0.250
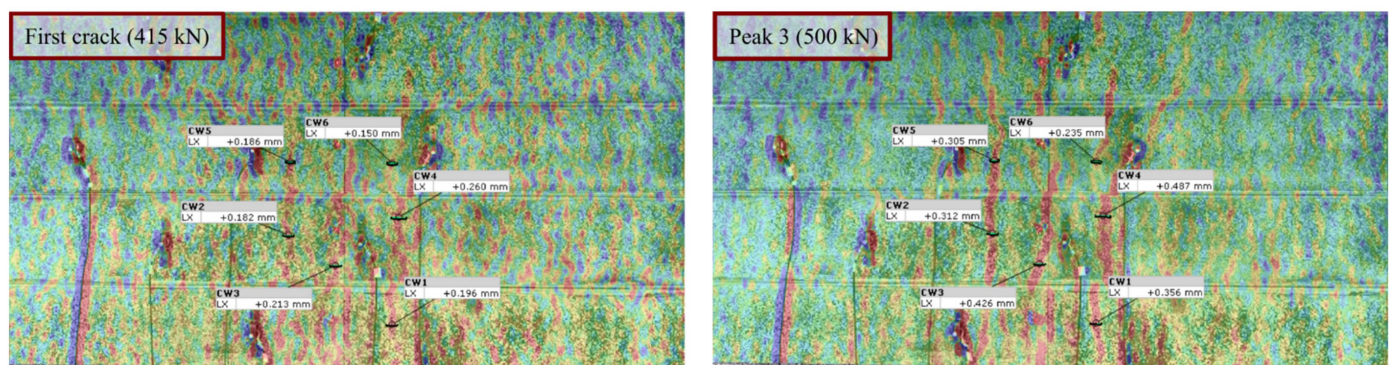
Figure 14. Measured crack widths at first crack (415 kN) and at Peak 3 (500 kN).

The Eurocode (EC) demand for maximal crack width in SLS [22] (w_{max} = 0.2 mm for this type of structure) has been chosen for comparison with the test results. This comparison shows that the stop criterion is not yet met at crack detection, but that all three load peaks at 500 kN exceed the criteria and that the structure must be considered damaged at this point. Through further analysis, it is found that the criterion is met at 468 kN (57% of the peak load). At the repeated loading to 500 kN, all crack widths exceed the criterion, and one of them does so by a factor of four. This corresponds well with the changed crack pattern of Figure 13 and supports that heavy damage has occurred by loading to 700 kN.

4.3. Acoustic Emission

MISTRAS AEwin software was used for AE measurement in OT test 2 [56]. Minor challenges were experienced due to pre-cracking of the compressive zone of the slab caused by the installation in the test setup. The significance of the pre-cracking may have been

increased by testing upside-down. While loading, AE events were acquired, not only from new crack formation and development, but also from the closure of pre-cracks in the compressive zone. The mix of AE events sources present difficulties for both early crack identification and the damage characterization with the load ratio and calm ratio. Consequently, it was not possible to gain useful results from the early crack identification, and these results are, therefore, not included. The AE results also depend on the pre-decided load levels in the applied loading protocol, which presents some limitations for the output assessment and damage characterization.

4.3.1. AE Activity Coupled to Loading Scheme

Figure 15 shows the global AE activity level as histograms. The achieved loading scheme is plotted on the secondary *y*-axis to couple the activity level to the load. The four subplots represent different parts and load levels of the loading scheme. Following the theory presented for the Kaiser effect, it would be expected to have limited AE activity until the previous load level. However, this is not the case due to the pre-cracking activity in the compressive zone. Consequently, this occurrence makes applying typical observations for the Kaiser and Felicity effect challenging. What can be observed is that the activity level is reduced towards the third cycle of each load level and that the unloading activity is insignificant for the 300 kN load level. At the 500 kN load level and higher, the unloading activity becomes predominant, indicating structural damage. Both of these observations are reflected in the later assessment of the calm ratio. The data presented in the Figure 15 graph is based on a real-time display on both a global and for individual sensor level.
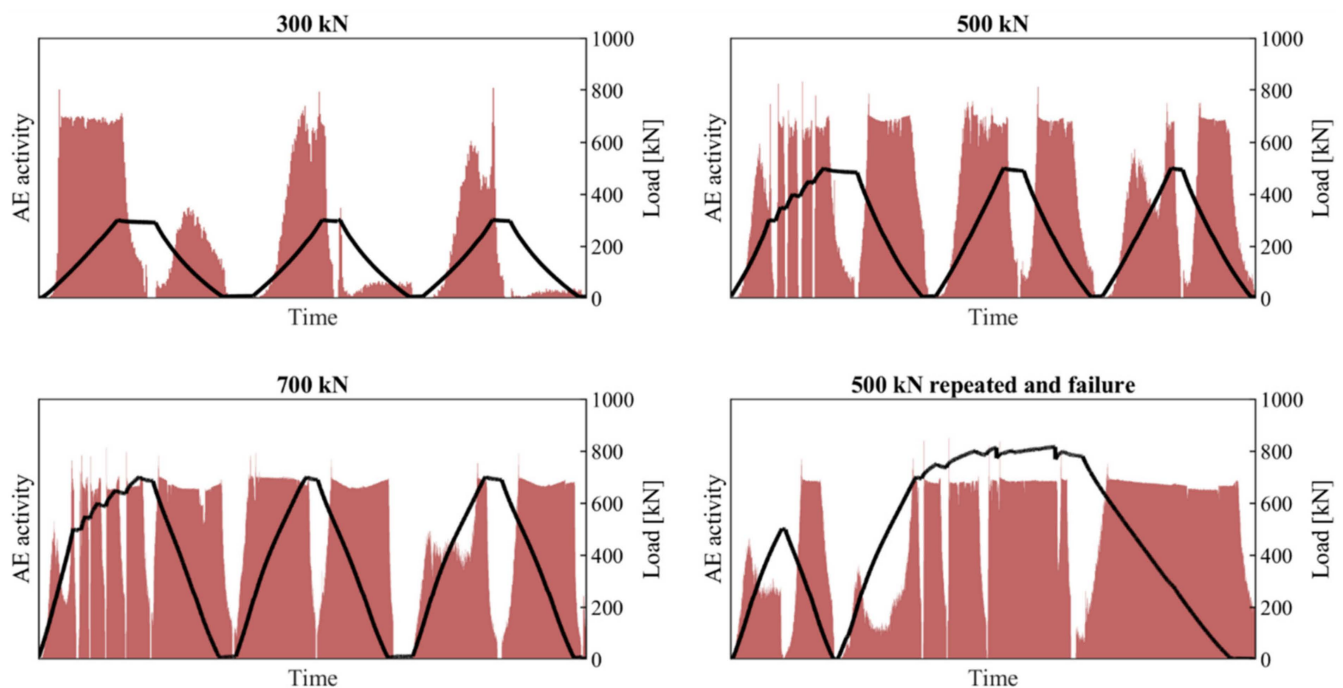
Figure 15. Global AE activity level for all load cycles.

4.3.2. Damage Characterization through Calm Ratio

Due to the challenges of observing the Kaiser effect, calculating load ratios does not make sense. As stated by Equation (1), the load ratio is given by the onset load level of significant AE activity over the maximum load of the load cycle; hence, the load ratios would indicate damage, even though the structure is not damaged. Therefore, the load ratio is not reliable for the damage assessment. Only the calm ratio is used in this paper. The calculation of the calm ratio is also affected by the additional AE activity. However, the ratio is more robust to such influence, and significant conclusions may still be drawn from

the results. Calculated calm ratios are given in Table 4. Results are provided for all sensors combined as well as every individual sensor. Sensor 15 was faulty and is not included.

Table 4. Calculated calm ratios for all sensors and all load levels.

Sensor No.	300 kN Cycle 1	Cycle 2	Cycle 3	500 kN Cycle 1	Cycle 2	Cycle 3	700 kN Cycle 1	Cycle 2	Cycle 3	500 kN Re.
All	0.22	0.12	*0.06*	0.47	0.47	*0.52*	0.49	0.48	*0.57*	0.63
1	0.26	0.16	*0.11*	0.56	0.56	*0.62*	0.53	0.55	*0.65*	0.73
2	0.29	0.13	*0.08*	0.66	0.61	*0.70*	0.54	0.57	*0.70*	0.82
3	0.33	0.12	*0.06*	0.47	0.46	*0.51*	0.49	0.46	*0.54*	0.63
4	0.30	0.13	*0.07*	0.57	0.51	*0.58*	0.50	0.48	*0.62*	0.69
5	0.35	0.13	*0.06*	0.54	0.49	*0.53*	0.48	0.54	*0.68*	0.70
6	0.21	0.11	*0.05*	0.29	0.33	*0.37*	0.47	0.44	*0.49*	0.53
7	0.09	0.11	*0.06*	0.52	0.53	*0.61*	0.55	0.55	*0.66*	0.72
8	0.27	0.12	*0.05*	0.33	0.35	*0.41*	0.48	0.42	*0.47*	0.52
9	0.26	0.12	*0.05*	0.49	0.48	*0.53*	0.50	0.44	*0.53*	0.62
10	0.20	0.11	*0.05*	0.22	0.27	*0.31*	0.46	0.41	*0.47*	0.48
11	0.21	0.12	*0.07*	0.38	0.39	*0.44*	0.47	0.47	*0.55*	0.58
12	0.18	0.11	*0.05*	0.27	0.31	*0.33*	0.46	0.45	*0.48*	0.45
13	0.23	0.13	*0.06*	0.23	0.26	*0.29*	0.43	0.38	*0.43*	0.42
14	0.08	0.12	*0.05*	0.13	0.20	*0.19*	0.45	0.50	*0.53*	0.33

The third load cycle is of significant importance for each load level since this is where the AE activities during loading are expected to stabilize. There is a low damage level for the 300 kN load level with a calm ratio between 0.05 and 0.11 (highest at sensors 1 and 2). For the 500 kN load level, the calm ratio has increased to between 0.2 and 0.7, which typically indicates light to heavy damage. Again the highest damage level is at sensors 1 and 2. For the 700 kN load level, the calm ratio is between 0.43 and 0.7. There is a tendency for a higher calm ratio near the loading point and the tensile surface of the slab (top side), which corresponds well with the expected and observed structural behavior. By comparison to the Rilem TC-212-ACD recommendation [45] using a calm ratio threshold of 0.2, the slab must be considered damaged at both 500 kN and 700 kN.

The calm ratios for the top sensors for the third load cycles are plotted in Figure 16 and compared to the DIC crack pattern. The bottom sensors are neglected since lower damage levels occurred in the compressive zone. It is seen how the damage characterization based on the calm ratio corresponds well with the DIC crack pattern.

4.3.3. AE Activity on Sensor Level

From Figure 16, it was observed that the damage characterization through the calm ratio corresponded well with the DIC crack pattern. Due to noticeable differences on the sensor activity level, it may also be relevant to view the AE activity results of individual sensors. Based on the presented results, it is most relevant to consider the 300 kN and 500 kN load levels. Figure 17 shows AE activity results for sensor 2 and sensor 10. Sensor 2 was placed almost directly above the loading point, and that is also where the highest damage level was expected and observed. Sensor 10 was located furthest away from the loading point, where lower damage levels were expected and observed. It is seen how the activity levels of the two sensors are comparable at the 300 kN load level but differ significantly at the 500 kN load level. At 500 kN, sensor 2 shows signs of damage, which is not yet the case for sensor 10.
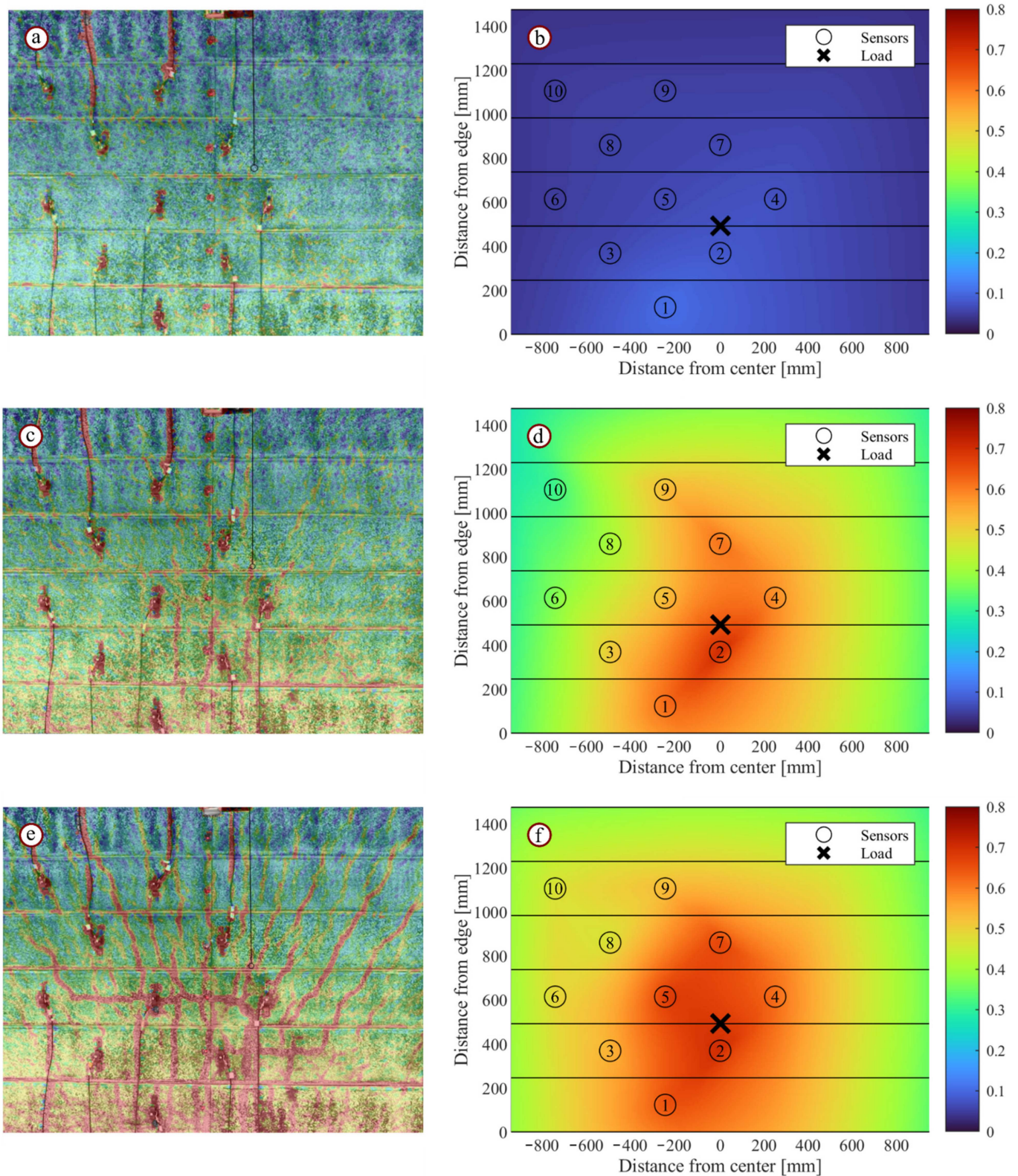
Figure 16. Crack pattern compared with surface plot of calm ratio at the third cycle of: (**a**,**b**) 300 kN, (**c**,**d**) 500 kN and (**e**,**f**) 700 kN. Only top sensors are included. Linear interpolation and zero-padding were applied to visualize the calm ratio surface plot; hence, only the contour within the confines of the sensor group is fully representative.
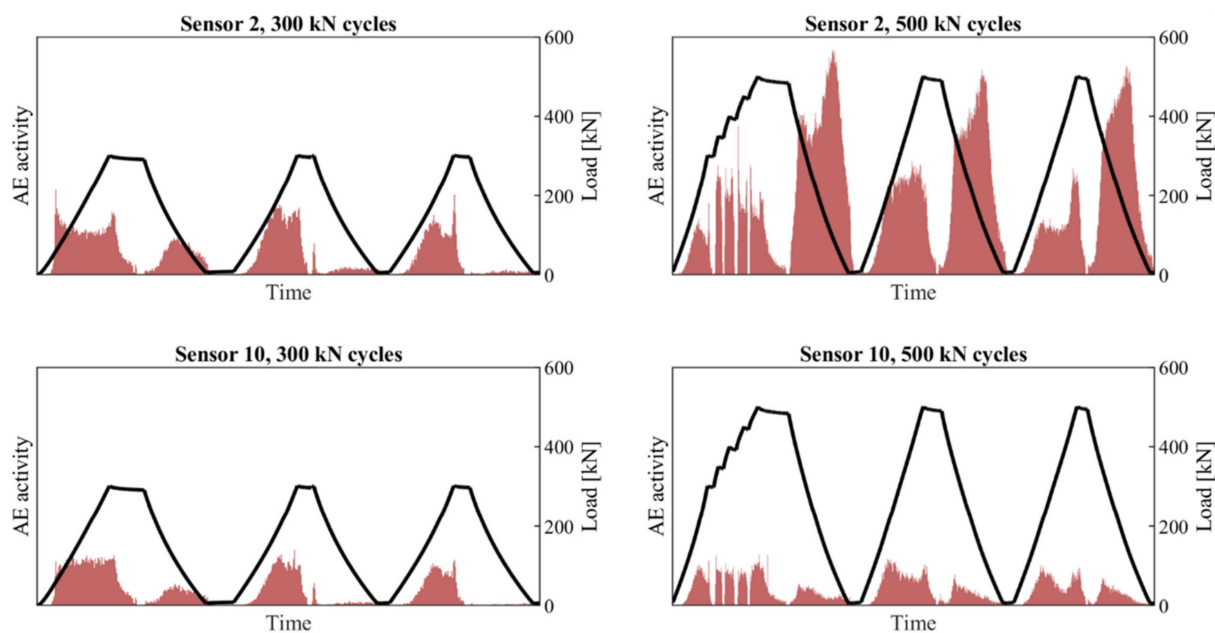
Figure 17. Damage development (activity) near sensor 2 and sensor 10.

5. Analysis and Discussion

The results show how qualitative observations can provide valuable information but not necessarily a definite stop criterion, while some stop criteria can be quantitatively monitored towards a threshold value. These different observations and quantitative measurements supplement each other and provide a higher information level and decision basis. This is illustrated through the individual evaluation of the measurements followed by a combined assessment.

5.1. Response Curve and Stiffness Change

Sufficient transverse redistribution of the load between the overturned T-section beams in the advanced OT-structure was observed in both tests, resulting in pronounced plate behavior and a high capacity. The response curve in Figure 11 supports this. It shows a gradual transfer to the plastic zone, which also fits well with later crack development results, where a gradual transfer from a partly cracked cross-section to a fully cracked cross-section is observed. The behavior and high capacity seem to indicate a capacity reserve in OT-slabs compared to typical theoretical evaluation methods.

Evaluation of individual loading cycles (Table 1) shows that the structure may be irreversibly damaged at 700 kN, which is later confirmed through other methods. Evaluation of stiffness change shows that all cycles of the 300 kN and 500 kN load levels are within an acceptable stiffness change. The stiffness criterion is reached in the increment between 500 kN and 700 kN, see Figure 12. Considering the test as a proof-loading situation, evaluating the response curve and stiffness change does not indicate damage at the 500 kN load level.

5.2. Digital Image Correlation

The DIC results show crack detection at 413 kN and 415 kN (see Table 2). For proof-loading application, it is preferable to have an algorithm which performs better than visual identification on the photograph. However, from current experience, noise makes it difficult to distinguish cracks from noise in a simple algorithm, and visual identification seems quite effective. Crack detection is preceded by indications of cracking activity (395 kN, 399 kN), but with the current DIC setup for full-field monitoring, earlier identification is not possible. DIC is dependent on camera resolution, camera distance, and other factors such as surface pattern composition and lighting. If a camera had been applied closer to the

surface in an area of interest, such crack indications would possibly have been identified as cracks. However, it was prioritized for the OT slab tests to have full-field monitoring and a camera distance comparable to earlier in-situ tests. Such prioritization may also be needed in proof-loading situations.

Crack pattern evaluations for OT test 2 (Figure 13) show how the cracks develop through each load level and how load history influences the crack pattern. This provides qualitative information about the structure and supports earlier results that significant damage occurs between the 500 kN and 700 kN load levels. Additional load levels could have provided more information in between these two load levels, but the test was performed using the entirely pre-defined loading protocol. This underlines that the loading protocol and the exact choice of load levels are essential aspects of proof-loading.

A comparison of measured crack widths from OT test 2 (Table 3) with the Eurocode SLS demand for maximum crack width (w_{max} = 0.2 mm for this type of structure) shows that the six monitored crack widths are less than the demand at crack detection (measured crack widths between 0.078 mm to 0.125 mm). However, on all three peaks of the 500 kN load level, some crack widths exceed the demand (measured crack widths between 0.081 mm to 0.283 mm). Considering the test as a proof-loading situation, using the EC demand as stop criterion, this results in test termination at a load of 468 kN, 53 kN past crack detection on the first cycle to 500 kN. This offers a sufficient margin between crack detection and test termination and even includes a hold of the load associated with the 50 kN load increments. Based on the results, and on results from previous studies [31], the system thus seems very applicable as a stand-alone monitoring method for effective stop criteria assessment. However, the pre-defined loading protocol would not be completed and thus proves insufficient for further evaluation (including AE). Therefore, it is relevant to discuss whether the loading protocol should be fully pre-defined or if input from monitoring sources should influence the applied load levels.

The results show that by application of the EC SLS threshold as a stop criterion, it is possible to monitor and control crack widths until the threshold is reached. Use of the threshold as a stop criterion is justified by its acceptance for the service limit state, why it should also be acceptable in proof-load testing. Note that the current study does not consider environmental classes, where the SLS threshold is defined by decompression.

5.3. Acoustic Emission

The AE results concerning damage identification correlate well with the other monitoring results, but also show some limitations of the current evaluation methods for in-situ testing applications. Due to testing upside-down, pre-cracking was observed in the compressive zone of OT test 2. During loading, closure of the pre-cracks generated AE events and mislead the results on early crack detection, the Kaiser effect, and the load ratio. The calm ratio results were also slightly affected by the unanticipated activity. However, compression zone cracks may also be present when field testing. The phenomenon is likely to occur from secondary activity caused by the road build-up, interaction between structural parts, or the loading procedure. It may affect the test results, but it provides valuable knowledge and more robustness for implementation in field-testing.

Considering AE activity vs. load (Figure 15), the third load cycle of each load level is of special interest. This is where the AE activity is expected to have stabilized. The results for the 300 kN load level show insignificant unloading activity in the third cycle, indicating that the structure is not yet damaged. At the third cycle of 500 kN and later, the unloading activity is more significant than the loading activity, which indicates that the structure is damaged at these stages. This representation of the results is useful since the plots are supported for real-time use in most software and provide valuable qualitative information.

Calm ratio results for the third load cycles show that OT test 2 must be considered damaged for both the 500 kN (calm ratios of 0.19 to 0.70) and 700 kN (calm ratios of 0.49 to 0.70) load levels, see Table 4. Following the recommendations of the Rilem TC-212-ACD with a calm ratio stop criterion of 0.2, the damage is not yet significant at 300 kN (calm

ratios of 0.05 to 0.11). From Figure 16, it is seen that the results correlate well with the DIC crack patterns and that the damage propagation of the crack pattern is reflected in the propagation of higher calm ratio values between 500 kN and 700 kN. Since there is a significant difference between AE sensors (e.g., calm ratio of 0.31 to 0.70 at 500 kN), this also means that the AE sensors must be placed in the critical zone or involve a larger array of sensors as applied in this study. Individual sensor results (Figure 17) support this, and it is seen how the activity/load plots vary significantly depending on the chosen sensor location. With sufficient knowledge of a given structure, a single sensor may provide applicable results if placed desirably (e.g., based on a diagnostic load level and related monitoring results combined with theoretical predictions). This may be highly relevant for in-situ testing, where the test time window is limited, and a cumbersome installation procedure can be a challenge.

Implementation in proof-load testing may pose a challenge since the AE calm ratio analysis is limited by the pre-defined loading protocol. For instance, between 300 kN (undamaged) and 500 kN (damaged), where the damage is assessed to occur, no additional load cycles are available, and thus no calm ratio data is present. Therefore, the use of the AE calm ratio in this way may not be directly suited for stand-alone application. It must be supported by other monitoring to define the load levels or involve additional load increments and levels (which may be undesirable due to a limited test time window). The calm ratio values are assessed to be artificially high due to unexpected activity, but as previously described, this also makes the results robust for future in-situ implementation. The recommendation from Rilem TC-212-ACD seems reasonable, although more testing with different loading protocols is required to verify the threshold and presented method further.

5.4. Proposal for Proof-Loading Procedure

Multiple stop criteria and structural observations have been evaluated as stand-alone methods for OT test 2. Evaluation of the response curve and associated stiffness change meet the corresponding stop criteria between 500 kN and 700 kN and do not indicate damage at the 500 kN load levels. Cracking was detected through DIC at 415 kN, and the chosen crack width stop criterion was met at 468 kN; hence, the results show damage before the 500 kN load peak. The AE results similarly show damage at 500 kN, but due to the pre-defined loading protocol does thus not indicate the damage occurrence as precisely as the DIC results. Based on the observations and experiences of the test, a proposal for combined use of DIC and AE has been created for future implementation in proof-load testing.

Instrumentation and preparation:

- A preliminary loading protocol is created based on available knowledge of the structure.
- DIC is used to cover the slab surface for real-time full-field measurements.
- A diagnostic load level load may be applied to provide additional prior knowledge.
- AE sensors are applied and positioned based on prior knowledge.
- The following load levels depend on each individual case, but as an example, the second load level could be below the expected cracking load, and the third load level could be the target load. Additional load levels could also be included for safety measures.
- Load increments should be applied in the first loading towards a higher load level.

During testing:

- Calm ratios are calculated after each load cycle and included in the decision basis for further loading.
- If no damage is detected, additional loading can be applied.
- Upon DIC crack detection, the loading is stopped, and the cracking load defines the peak load of the current load level with three load cycles, thus adjusting the pre-defined loading protocol.

- The calm ratio can thus be evaluated at crack detection while measuring crack widths at crack detection, and calculated calm ratios provide the decision basis for continued loading. If the target load is reached before exceeding other stop criteria, the test is terminated.

The presented proposal requires further testing before implementation into proof-load testing can be done; however, it serves as a solid basis for further research. The AE results on sensor level also suggest that if the sensors are correctly placed in the critical zone, analysis can be done with a lower number of sensors. This could be useful for field implementation, where the use of a system with many sensors can be both time-consuming to apply and expensive.

5.5. Perspective towards Previous Studies

The authors are not aware of any previous studies which have applied the combined methodology in this way on concrete slabs of comparable size. Most studies using DIC and AE involve small-scale experiments [15,49–52] and apply entirely different methods. The study of Zhang et al. (2020) [39] is more comparable with large-scale tests on concrete bridge girders; however, the focus was more on crack kinematics and localization. The study presented in this paper is thus novel in terms of the practical and optimized use of the methods and its perspective towards field implementation. The use of qualitative observations increases the method's robustness; hence the influence and significance of environmental conditions may be reduced. The results may contribute to increased use of proof-load testing for structural evaluation of existing bridges in the future.

6. Conclusions

This paper considers the combined use of 2D digital image correlation and acoustic emission for stop criteria identification associated with proof-load testing. Two large-scale laboratory tests were performed on OT slabs, one as a preliminary test and one monitored by both DIC and AE. The monitoring systems were assessed as stand-alone systems, and the combined methodology was evaluated to provide a proposal for future implementation in field testing. The DIC results included full-field plots, an investigation of the time of crack detection, and monitoring of crack widths. The AE results included analyses of AE activity vs. load, along with damage characterization through calm ratio. The following can be concluded based on the presented research:

- The loading protocol was successfully applied, but the results showed that a fully pre-defined loading protocol might be insufficient.
- Evaluation of the response curve, stiffness change, and DIC crack patterns indicated damage occurrence between 500 kN and 700 kN.
- Crack were detected by DIC at 413–415 kN (crack widths between 0.078 mm to 0.125 mm), whereas the chosen stop criterion (EC SLS demand w_{max} = 0.2 mm) was met at 468 kN, thus leaving a sufficient margin between crack detection and activation of the criterion (53 kN).
- Qualitative AE analysis of activity vs. load showed that OT test 2 was not yet damaged at 300 kN, but that damage was present at the 500 kN load level and higher. This was supported by quantitative analysis of calm ratio (comparison to the Rilem TC-212-ACD).
- Since the AE calm ratio method was bound to the pre-defined loading protocol, it was impossible to determine the damage state between the 300 kN load level and the 500 kN load level.
- The combined use of DIC and AE thus seems to provide a robust stop criteria evaluation method with stop criteria identification before conventional methods. However, the study also shows that DIC can be effectively applied as a stand-alone method, while AE may benefit further from input from other monitoring sources.
- This insight enabled a proposal for how to optimize the combined methodology for proof-load testing. The basis for the approach is that the pre-defined loading protocol can be updated during loading, e.g., at DIC crack detection, which may define the

peak load of the current load cycle. Consequently, both qualitative and quantitative measurements are included, and the damage assessment through AE is supported by optimal load levels.

Testing upside-down presented some challenges in the analysis of the AE results. Unexpected AE activity made it difficult to observe early crack detection, the Kaiser effect, and to calculate the load ratio. However, such phenomenon may also be present in in-situ structures, and the study, therefore, provides valuable and robust results for further implementation in field testing. The combined testing was done on one large-scale element, and can thus only support the potential of the methodology. Consequently, more testing is needed to verify the method further.

Author Contributions: Conceptualization, C.O.C., J.W.S.; methodology, C.O.C., J.W.S.; software, C.O.C., J.W.S.; validation, C.O.C., J.W.S., F.Z., G.Z.G.; formal analysis, C.O.C., F.Z., G.Z.G.; investigation, C.O.C., J.W.S., F.Z., G.Z.G.; resources, J.W.S.; data curation, C.O.C., F.Z., G.Z.G.; writing—original draft preparation, C.O.C., J.W.S.; writing—review and editing, C.O.C., J.W.S., F.Z., G.Z.G., E.O.L.L., P.G.; visualization, C.O.C.; supervision, J.W.S., E.O.L.L., P.G.; project administration, J.W.S., P.G.; funding acquisition, J.W.S. All authors have read and agreed to the published version of the manuscript.

Institutional Review Board Statement: Not applicable.

Informed Consent Statement: Not applicable.

Data Availability Statement: All data and information needed for the evaluations discussed are provided in the paper.

Conflicts of Interest: The authors declare no conflict of interest.

References

1. Aguilar, C.V.; Jauregui, D.V.; Newtson, C.M.; Weldon, B.D.; Cortez, T.M.; Information, R. Load Rating a Prestressed Concrete Double T-Beam Bridge without Plans by Field Testing. *Transp. Res. Rec. J. Transp. Res. Board* **2015**, *2522*, 90–99. [CrossRef]
2. Lantsoght, E.O.L.; Koekkoek, R.T.; Hordijk, D.; De Boer, A. Towards standardisation of proof load testing: Pilot test on viaduct Zijlweg. *Struct. Infrastruct. Eng.* **2017**, *14*, 365–380. [CrossRef]
3. Faber, M.H.; Val, D.V.; Stewart, M.G. Proof load testing for bridge assessment and upgrading. *Eng. Struct.* **2000**, *22*, 1677–1689. [CrossRef]
4. Halicka, A.; Hordijk, D.A.; Lantsoght, E.O. Rating of Concrete Road Bridges with Static Proof Load Tests. In *SP-323: Evaluation of Concrete Bridge Behavior through Load Testing-International Perspectives*; American Concrete Institute: Farmington Hills, MI, USA, 2018; Volume 323, pp. 3.1–3.16.
5. Gosbell, K.B.; Stevens, L.K. Test Loading of a Full Scale Bridge. *Aust. Road Res. Board Conf. Proc.* **1968**, *4*, 2018–2041.
6. Goodpasture, D.W.; Burdette, E.G. Full Scale Tests to Failure of Four Highway Bridges. *Am. Railw. Eng. Assoc.* **1973**, *74*, 454–473.
7. Isaksen, H.R.; Kanstad, T.; Olsen, P.-E. *Prøvebelastning Av Bru Nr 02-1234 Smedstua Bru*; Statens Vegvesen: Oslo, Norway, 1998.
8. Zhang, J.; Peng, H.; Cai, C.S. Field Study of Overload Behavior of an Existing Reinforced Concrete Bridge under Simulated Vehicle Loads. *J. Bridg. Eng.* **2011**, *16*, 226–237. [CrossRef]
9. Zhang, J.; Peng, H.; Cai, C.S. Destructive Testing of a Decommissioned Reinforced Concrete Bridge. *J. Bridg. Eng.* **2013**, *18*, 564–569. [CrossRef]
10. Lantsoght, E.O.L.; van der Veen, C.; de Boer, A.; Hordijk, D.A. State-of-the-Art on Load Testing of Concrete Bridges. *Eng. Struct.* **2017**, *150*, 231–241. [CrossRef]
11. Lantsoght, E.O.L. (Ed.) *Load Testing of Bridges: Current Practice and Diagnostic Load Testing*, 1st ed.; CRC Press: Boca Raton, FL, USA, 2019; ISBN 9780367210823.
12. Alampalli, S.; Frangopol, D.M.; Grimson, J.; Kosnik, D.; Halling, M.; Lantsoght, E.; Weidner, J.S.; Yang, D.Y.; Zhou, Y.E. *Primer on Bridge Load Testing*; Transport; Transportation Research Board (TRB): Washington, DC, USA, 2019; ISBN 0097-8515.

13. Garnica, G.I.Z.; Zhang, F.; Yang, Y.; van der Veen, C.; Lantsoght, E.O.L.; Naaktgeboren, M.; Fennis, S.A.A.M. Monitoring Structural Responses during Proof Load Testing of Reinforced Concrete Bridges: A Review. In Proceedings of the Bridge Maintenance, Safety, Management, Life-Cycle Sustainability and Innovations (IABMAS), Sapporo, Japan, 28 June–2 July 2020.

14. Omondi, B.; Aggelis, D.G.; Sol, H.; Sitters, C. Improved crack monitoring in structural concrete by combined acoustic emission and digital image correlation techniques. *Struct. Health Monit.* **2016**, *15*, 359–378. [CrossRef]

15. Alam, S.Y.; Loukili, A.; Grondin, F.; Rozière, E. Use of the digital image correlation and acoustic emission technique to study the effect of structural size on cracking of reinforced concrete. *Eng. Fract. Mech.* **2015**, *143*, 17–31. [CrossRef]

16. Schmidt, J.W.; Halding, P.S.; Jensen, T.W.; Engelund, S. High Magnitude Loading of Concrete Bridges. *SP-323 Eval. Concr. Bridge Behav. Thr. Load Test.-Int. Perspect.* **2018**, *323*, 9.1–9.20.

17. Vejdirektoratet (The Danish Road Directorate). *Vejledning Til Belastnings-Og Beregningsgrundlag*; The Danish Road Directorate: Copenhagen, Denmark, 2010.

18. Vejdirektoratet (The Danish Road Directorate). *Annex A: Lastmodeller for Klassificering Og Bæreevnevurdering (Models of Special Vehicles for Road Bridges)*; The Danish Road Directorate: Copenhagen, Denmark, 2010.

19. DAfStb. *DAfStb-Guideline: Load Tests on Concrete Structures*; Deutscher Ausschuss für Stahlbeton: Berlin, Germany, 2000.

20. ACI Commitee 437. *Code Requirements for Load Testing of Existing Concrete Structures (ACI 437.2M-13)*; American Concrete Institute: Farmington Hills, MA, USA, 2013.

21. Lantsoght, E.O.L.; Yang, Y.; Van Der Veen, C.; Hordijk, D.A.; De Boer, A. Stop Criteria for Flexure for Proof Load Testing of Reinforced Concrete Structures. *Front. Built Environ.* **2019**, *5*, 47. [CrossRef]

22. European Committee for Standardization. *EN 1992-1-1, Eurocode 2: Design of Concrete Structures-Part 1-1: General Rules and Rules for Buildings*; European Committee for Standardization: Brussels, Belgium, 2008.

23. Lantsoght, E.O.L.; Yang, Y.; Tersteeg, R.H.D.; Van Der Veen, C.; De Boer, A. Development of Stop Criteria for Proof Loading. In *Life-Cycle of Engineering Systems: Emphasis on Sustainable Civil Infrastructure, Proceedings of the 5th International Symposium on Life-Cycle Engineering, IALCCE 2016, Delft, The Netherlands, 16–19 October 2016*; CRC Press: Boca Raton, FL, USA, 2016; ISBN 9781138028470.

24. Lantsoght, E.O.L.; Yang, Y.; van der Veen, C.; de Boer, A.; Hordijk, D.A. Beam Experiments on Acceptance Criteria for Bridge Load Tests. *ACI Struct. J.* **2017**, *114*, 1031. [CrossRef]

25. Lantsoght, E.O.L.; van der Veen, C.; Hordijk, D.A. Proposed Stop Criteria for Proof Load Testing of Concrete Bridges and Verification. In Proceedings of the Life-Cycle Analysis and Assessment in Civil Engineering: Towards an Integrated Vision—6th International Symposium on Life-Cycle Civil Engineering, IALCCE 2018, Belgium, Ghent, 28–31 October 2018.

26. Lantsoght, E.O.L.; Yang, Y.; Van Der Veen, C.; De Boer, A.; Hordijk, D.A. Determination of Loading Protocol and Stop Criteria for Proof Loading with Beam Tests. In Proceedings of the High Tech Concrete: Where Technology and Engineering Meet-Proceedings of the 2017 fib Symposium, Maastricht, The Netherlands, 12–14 June 2017.

27. Lantsoght, E.O.L.; Yang, Y.; Van Der Veen, C.; Hordijk, D.A. Stop Criteria for Proof Load Tests Verified with Field and Laboratory Testing of the Ruytenschildt Bridge Ruytenschildt Field Test. In Proceedings of the IABSE Conference, Kongens Lyngby, Denmark, 25–26 June 2018; pp. 1–8.

28. Benitez, K.; Lantsoght, E.O.L.; Yang, Y. Development of a Stop Criterion for Load Tests Based on the Critical Shear Displacement Theory. In Proceedings of the 6th International Symposium on Life-Cycle Civil Engineering, IALCCE 2018, Ghent, Belgium, 28–31 October 2018; pp. 145–152.

29. Garnica, G.I.Z.; Lantsoght, E.O.L. Stop Criteria for Proof Load Testing of Reinforced Concrete Structures. In Proceedings of the 13th Fib International PhD Symposium in Civil Engineering, Paris, France, 26–28 August 2020.

30. Schmidt, J.W.; Thöns, S.; Kapoor, M.; Christensen, C.O.; Engelund, S.; Sørensen, J.D. Challenges Related to Probabilistic Decision Analysis for Bridge Testing and Reclassification. *Front. Built Environ.* **2020**, *6*, 14. [CrossRef]

31. Christensen, C.O.; Schmidt, J.W.; Halding, P.S.; Kapoor, M.; Goltermann, P. Digital Image Correlation for Evaluation of Cracks in Reinforced Concrete Bridge Slabs. *Infrastructures* **2021**, *6*, 99. [CrossRef]

32. Halding, P.S.; Schmidt, J.W.; Jensen, T.W.; Henriksen, A.H. Structural Response of Full-Scale Concrete Bridges Subjected to High Load Magnitudes. In Proceedings of the SMAR, Zürich, Switzerland, 13–15 September 2017.

33. Halding, P.S.; Schmidt, J.W.; Christensen, C.O. DIC-Monitoring of Full-Scale Concrete Bridge Using High-Resolution Wide-Angle Lens Camera. In Proceedings of the 9th International Conference on Bridge Maintenance, Safety and Management, Melbourne, Australia, 9–13 July 2018; pp. 1492–1499.

34. Halding, P.S.; Christensen, C.O.; Schmidt, J.W. Surface Rotation Correction and Strain Precision of Wide-Angle 2D DIC for Field Use. *J. Bridg. Eng.* **2019**, *24*, 04019008. [CrossRef]

35. Tan, X.; Abu-Obeidah, A.; Bao, Y.; Nassif, H.; Nasreddine, W. Measurement and Visualization of Strains and Cracks in CFRP Post-Tensioned Fiber Reinforced Concrete Beams Using Distributed Fiber Optic Sensors. *Autom. Constr.* **2021**, *124*, 103604. [CrossRef]

36. Merzbacher, C.I.; Kersey, A.D.; Friebele, E.J. Fiber Optic Sensors in Concrete Structures: A Review. *Smart Mater. Struct.* **1996**, *5*, 196–208. [CrossRef]

37. Helmi, K.; Taylor, T.; Zarafshan, A.; Ansari, F. Reference Free Method for Real Time Monitoring of Bridge Deflections. *Eng. Struct.* **2015**, *103*, 116–124. [CrossRef]

38. Maaskant, R.; Alavie, A.T.; Measures, R.M.; Ohn, M.M.; Karr, S.E.; Glennie, D.J.; Wade, C.; Tadros, G.; Rizkalla, S. Fiber Optic Bragg Grating Sensor Network Installed in a Concrete Road Bridge. *Proc. SPIE* **1994**, *2191*, 457–465. [CrossRef]

39. Zhang, F.; Garnica, G.I.Z.; Yang, Y.; Lantsoght, E.; Sliedrecht, H. Monitoring Shear Behavior of Prestressed Concrete Bridge Girders Using Acoustic Emission and Digital Image Correlation. *Sensors* **2020**, *20*, 5622. [CrossRef] [PubMed]

40. Schreier, H.; Orteu, J.J.; Sutton, M.A. *Image Correlation for Shape, Motion and Deformation Measurements: Basic Concepts, Theory and Applications*; Springer Science & Business Media: Berlin/Heidelberg, Genmany, 2009; ISBN 9780387787466.

41. Sutton, M.A.; Matta, F.; Rizos, D.; Ghorbani, R.; Rajan, S.; Mollenhauer, D.H.; Schreier, H.W.; Lasprilla, A.O. Recent Progress in Digital Image Correlation: Background and Developments since the 2013 W M Murray Lecture. *Exp. Mech.* **2017**, *57*, 1–30. [CrossRef]

42. Christensen, C.O.; Lantsoght, E.O.L.; Schmidt, J.W. Quantification of Digital Image Correlation Applicability Related to In-Situ Proof Load Testing of Bridges. In Proceedings of the SMAR 2019—Fifth Conference on Smart Monitoring, Assessment and Rehabilitation of Civil Structures, Potsdam, Germany, 27–29 August 2019; pp. 1–8.

43. Di Benedetti, M.; Nanni, A. Acoustic Emission Intensity Analysis for In Situ Evaluation of Reinforced Concrete Slabs. *J. Mater. Civ. Eng.* **2014**, *26*, 6–13. [CrossRef]

44. Ohtsu, M.; Uchida, M.; Okamoto, T.; Yuyama, S. Damage Assessment of Reinforced Concrete Beams Qualified by Acoustic Emission. *ACI Struct. J.* **2002**, *99*, 411–417. [CrossRef]

45. Ohtsu, M.; Shiotani, T.; Shigeishi, M.; Kamada, T.; Yuyama, S.; Watanabe, T.; Suzuki, T.; van Mier, J.G.M.; Vogel, T.; Grosse, C.; et al. Recommendation of RILEM TC 212-ACD: Acoustic Emission and Related NDE Techniques for Crack Detection and Damage Evaluation in Concrete: Measurement Method for Acoustic Emission Signals in Concrete. *Mater. Struct. Constr.* **2010**, *43*, 1183–1186. [CrossRef]

46. Yang, Y.; Hordijk, D.A.; De Boer, A. Acoustic Emission Measurement in the Proof Loading of an Existing Bridge Affected by ASR. In Proceedings of the Life-Cycle of Engineering Systems: Emphasis on Sustainable Civil Infrastructure—5th International Symposium on Life-Cycle Engineering, IALCCE 2016, Delft, The Netherlands, 16–19 October 2016.

47. Tsangouri, E.; Remy, O.; Boulpaep, F.; Verbruggen, S.; Livitsanos, G.; Aggelis, D.G. Structural Health Assessment of Prefabricated Concrete Elements Using Acoustic Emission: Towards an Optimized Damage Sensing Tool. *Constr. Build. Mater.* **2019**, *206*, 261–269. [CrossRef]

48. Grosse, C.U.; Ohtsu, M. *Acoustic Emission Testing: Basics for Research-Applications in Civil Engineering*; Springer Nature: Berlin/Heidelberg, Germany, 2008.

49. Zhang, H.; Fu, D.; Song, H.; Kang, Y.; Huang, G.; Qi, G.; Li, J. Damage and Fracture Investigation of Three-Point Bending Notched Sandstone Beams by DIC and AE Techniques. *Rock Mech. Rock Eng.* **2015**, *48*, 1297–1303. [CrossRef]

50. Flament, C.; Salvia, M.; Berthel, B.; Crosland, G. Local Strain and Damage Measurements on a Composite with Digital Image Correlation and Acoustic Emission. *J. Compos. Mater.* **2016**, *50*, 1989–1996. [CrossRef]

51. Lacidogna, G.; Piana, G.; Accornero, F.; Carpinteri, A. Multi-Technique Damage Monitoring of Concrete Beams: Acoustic Emission, Digital Image Correlation, Dynamic Identification. *Constr. Build. Mater.* **2020**, *242*, 118114. [CrossRef]

52. Alam, S.Y.; Saliba, J.; Loukili, A. Fracture Examination in Concrete through Combined Digital Image Correlation and Acoustic Emission Techniques. *Constr. Build. Mater.* **2014**, *69*, 232–242. [CrossRef]

53. GOM. GOM Correlate Professional 2018. Available online: https://www.gom.com/en/products/gom-suite/gom-correlate-pro (accessed on 1 March 2022).

54. Blaber, J.; Adair, B.; Antoniou, A. Ncorr: Open-Source 2D Digital Image Correlation Matlab Software. *Exp. Mech.* **2015**, *55*, 1105–1122. [CrossRef]

55. MISTRAS. *R6I-AST Sensor*; MISTRAS Gr. Inc.: Princeton Junction, NJ, USA, 2008.

56. MISTRAS. *AEwin SOFTWARE, Installation, Operation and User's Reference Manual*; Products & Systems Division: Princeton Junction, NJ, USA, 2011.

57. Bedford, A.; Drumheller, D. *Introduction to Elastic Wave Propagation*; John Wiley Sons: Singapore, 1994.